Internal wave excitation by a vertically oscillating sphere

By MORRIS R. FLYNN, KRISTJAN ONU
AND BRUCE R. SUTHERLAND

Department of Mathematical and Statistical Sciences, University of Alberta,
Edmonton, AB, Canada T6G 2G1

The properties of waves generated by a vertically oscillating sphere in a uniformly stratified fluid are examined both theoretically and experimentally. Existing predictions for the wave amplitude and phase structure are modified to account for the effects of viscous attenuation. As with waves generated by an oscillating cylinder, the main effect of attenuation is to broaden the two peaks of the amplitude envelope on either flank of the wave beam so that far from the sphere the wave beam exhibits a single peak with a maximum along the centreline. The transition distance from bimodal to unimodal wave beam structure is shown to occur closer to the source than the corresponding distance calculated for the oscillating circular cylinder. For laboratory experiments, a recently developed 'synthetic schlieren' method is adapted so that quantitative measurements may be made of an axisymmetric wave field. This non-intrusive technique allows us to evaluate the amplitude of the waves everywhere in space and time. Experiments are performed to examine the amplitude of waves generated by small and large spheres oscillating with a range of amplitudes and frequencies. The wave amplitude is found to scale linearly with the oscillation amplitude A for A/a as large as 0.27, where a is the radius of the sphere. Generally good agreement between theory and experiment is found for the small sphere experiments. However, the theory overpredicts both the amplitude and the bimodal-to-unimodal transition distance for waves generated by the large sphere.

1. Introduction

Just as water waves may be generated by an object bobbing vertically at the surface, so may internal waves be generated by an oscillating body within a density stratified fluid. However, the dynamics of the latter are quite different. For example, whereas surface waves radiate as concentric rings from a localized periodic source, internal waves are well known to propagate along wave beams with fixed angle to the vertical (Mowbray & Rarity 1967a; Lighthill 1978). A periodically oscillating cylinder which is oriented with its axis horizontal generates four wave beams that form a 'St Andrew's Cross' pattern with the cylinder at the centre of the cross. Similarly, an oscillating sphere creates waves in the form of two cones lying above and below the sphere. The angle, Θ, of the wave beams to the vertical is determined entirely by the ratio of the frequency of oscillation of the source to the background buoyancy frequency.

Earlier experimental and theoretical investigations into internal waves generated by moving bodies examined the phase structure, but not the amplitude of the waves

(Mowbray & Rarity 1967*a*, *b*; Stevenson 1969). The theoretical basis for examining the detailed structure of inviscid small-amplitude internal waves has been established using both Fourier transforms (Lighthill 1960, 1967) and Green's functions (Voisin 1991). Conformal mapping and analytic continuation methods have been employed to examine wave beams generated by the simple two-dimensional geometry of an oscillating cylinder with circular and elliptical cross-sections (Appleby & Crighton 1986; Hurley 1997). These studies predict that the along-beam amplitude is constant if viscous effects are ignored. However, the theories predict infinite velocities along the two lines tangential to the cylinder which form an angle Θ with the vertical.

   This unphysical result is remedied by including the effects of viscous attenuation. Assuming viscous effects remain relatively small, we can adopt the boundary-layer approximation of Thomas & Stevenson (1972) to derive a linear partial differential equation from which analytic solutions can be derived. Applied to the case of an oscillating circular cylinder, Hurley & Keady (1997) showed that the two peaks in the amplitude envelope eventually merge to form a single peaked wave beam (Makarov, Neklyudov & Chashechkin 1990). In general, their predictions agree well with experimental measurements (Sutherland *et al.* 1999). Small discrepancies between the measured and predicted beam width are due to the presence of viscous boundary layers that surround the cylinder; these dynamics are neglected by theory. For sufficiently large-amplitude and low-frequency oscillations, a nonlinear phenomenon is also observed: the waves interact with the viscous boundary layer in a way that generates secondary wave beams with double the frequency of oscillation of the source (Sutherland & Linden 2002).

   Less is known about the amplitude of internal waves generated from an oscillating sphere. In inviscid theory, the waves radiate along cones, which have a cross-sectional area that increases linearly with distance from the source. Hence, even in the absence of viscous attenuation, conservation of energy flux requires that the amplitude decreases as $r^{-1/2}$, where r is the radial distance from the centre of the sphere. This behaviour is indeed predicted by inviscid linear theories (Appleby & Crighton 1987; Voisin 1991). As with inviscid theories for internal waves generated by oscillating cylinders, waves generated by oscillating spheres are predicted to have unphysically large velocities where the wave beams are tangent to the sphere. In part of the work presented here, we follow the boundary-layer approximation of Thomas & Stevenson (1972) and use the method outlined by Lighthill (1978, §4.10), to include the effects of viscous attenuation.

   Until recently, experiments measuring internal wave amplitudes have for the most part been limited to studies of large-amplitude waves generated by flow over topography. In part, this is because dye and particle tracking techniques are limited to visualizing motions larger than the size of the dye lines and particles themselves. With the notable exception of Thomas & Stevenson (1972), in laboratory studies of internal waves generated by oscillating cylinders and spheres, typically the displacements are so small that they are visualized using schlieren techniques, which are non-intrusive and sensitive to small disturbances in stratified fluids (e.g. Mowbray 1967; Stevenson 1969). There are a variety of experimental set-ups, but all schlieren techniques are linked by exploiting the fact that light is bent to a greater or lesser degree as density gradients in the fluid strengthen or weaken, respectively.

   Classical schlieren techniques are useful as a qualitative tool, enabling us to visualize wave crests and troughs but providing no amplitude information. Quantitative schlieren methods have been developed in the past decade with the aid of digital enhancement (Irvin & Ross 1991; Greenberg, Klimek & Buchele 1995; Dalziel,

Hughes & Sutherland 2000). 'Synthetic schlieren' has proved to be particularly useful for measuring the amplitude of waves generated by an oscillating circular and elliptical cylinder (Sutherland *et al.* 1999, 2000; Sutherland & Linden 2002). In these experiments, a camera is focused through a stratified salt-water solution upon an image of horizontal black lines. Internal waves are generated from an oscillating cylinder spanning the tank and with its axis along the line of sight of the camera. The waves stretch and compress isopycnal (constant density) surfaces, thus bending the light reaching the camera and distorting the image. Under the assumption that the wave beams are uniform along the line of sight of the camera, the amplitude of the waves is easily calculated from the measured displacement of lines in the distorted image.

The quantitative use of synthetic schlieren has so far been used for two-dimensional geometries. This paper demonstrates how synthetic schlieren may be extended to measure three-dimensional but axisymmetric internal wave fields. We perform a series of laboratory experiments in which internal waves are generated by a vertically oscillating sphere in uniformly stratified fluid. The waves are again visualized by focusing a camera through the tank upon an image of horizontal black lines and the displacement of lines due to the waves is measured. Assuming the waves are axisymmetric about the vertical axis, the amplitude of the wave field can be reconstructed from the displacements through matrix inversion methods, a simple adaption of inverse tomography.

In §2, we adapt the inviscid theory of Voisin (1991) to include the effects of viscous attenuation for wave beams generated by an oscillating sphere. The experimental set-up and the qualitative and quantitative use of synthetic schlieren is described in §3. The techniques are applied to the experimental data in §4 and we compare the results to the theoretical predictions given in §2. We summarize our results in §5.

2. Theory

It is assumed that the fluid surrounding the sphere is Boussinesq, meaning that density variations are negligible except for their effect upon buoyancy forces. This assumption is justifiable for the experiments discussed in §3.1 because the total density change over the height of the tank is approximately 5%. For such salt-stratified solutions, the squared buoyancy frequency is defined by $N^2 = -(g/\rho_0)\,\mathrm{d}\bar{\rho}/\mathrm{d}z$, where g is the acceleration due to gravity ($\simeq 980\,\mathrm{cm\,s^{-2}}$), ρ_0 is a characteristic value of density ($\simeq 1.0\,\mathrm{g\,cm^{-3}}$ for water), and $\bar{\rho}(z)$ is the fluid's initial unperturbed density as a function of height, z.

We consider the case in which the sphere oscillates at a constant frequency, ω, which is strictly less than N. Thus, the sphere generates propagating internal waves that transport energy away from the source. The angle formed between the lines of constant phase and the vertical, $\Theta \equiv \cos^{-1}(\omega/N)$, lies between $0°$ and $90°$. We further assume that the waves generated by the oscillating sphere are axisymmetric, emanating as a pair of cones above and below the sphere, as illustrated in figure 1(*a*).

2.1. *Inviscid theory*

The structure of internal wave beams generated by a pulsating and a vertically oscillating sphere in inviscid uniformly stratified fluid, was first derived by Appleby & Crighton (1987). Assuming free-slip boundary conditions on the surface of the sphere, they derived their formulae by solving an elliptic partial differential equation in the case of evanescent wave excitation (with oscillation frequency ω greater than the
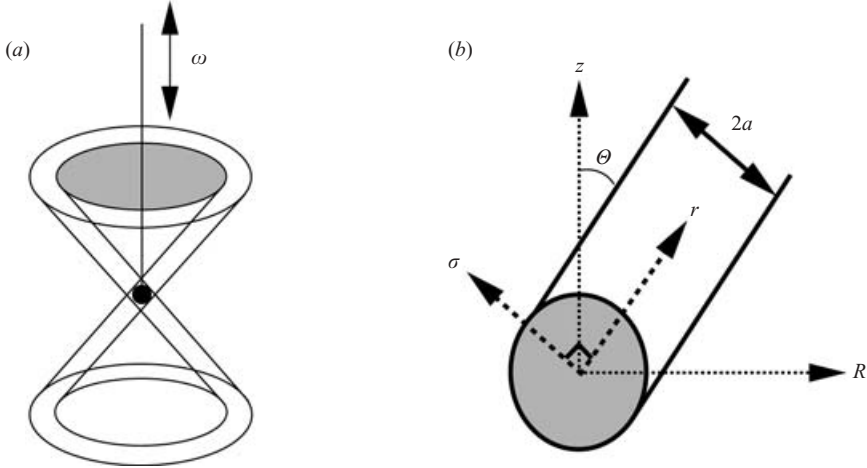
FIGURE 1. (*a*) Geometry of the wave cones generated by an oscillating sphere in a uniformly stratified medium. (*b*) Coordinate system used to model the upward-propagating cone.

buoyancy frequency N). Their result was extended to the case $\omega < N$ through analytic continuation. Though simple in expression, their formulae involved variables expressed in a non-intuitive coordinate system.

Using a Green's function approach, Voisin (1991) determined the structure of internal wave beams generated by a pulsating sphere. His result was identical to that of Appleby & Crighton (1987), but expressed in the more intuitive across-beam (σ) and radial (ϱ) coordinate system.

Likewise, a formula for inviscid internal wave beams generated by a vertically oscillating sphere can be written in (σ, ϱ)-coordinates. Using cylindrical coordinates, we define the axisymmetric streamfunction amplitude $\psi(R, z)$ so that the radial, u_R, and vertical, u_z, components of the velocity field are given by

$$u_R = -\frac{\partial \psi}{\partial z} \tag{2.1}$$

and

$$u_z = \frac{1}{R}\frac{\partial(R\psi)}{\partial R}. \tag{2.2}$$

Here, R is the horizontal radial coordinate and z is the vertical coordinate.

We combine the formulae of Appleby & Crighton (1987) and Voisin (1991), and use the result in Appendix A to convert from the velocity potential (used by Voisin 1991) to streamfunction, ψ. Thus, for the upward-propagating wave cone, we find

$$\psi(\varrho, \sigma)|_{\nu=0} \sim \begin{cases} iAaN\left(\dfrac{\cos^3 \Theta}{\sin \Theta}\right)^{1/2}\left(\dfrac{a}{\varrho}\right)^{1/2}\exp\left[i\tfrac{3}{2}\cos^{-1}\left(\dfrac{\sigma}{a}\right)\right] & |\sigma| < a, \\[3mm] -iAaN\cos\Theta\left(1 - \dfrac{\cos^2 \vartheta}{\cos^2 \Theta}\right)^{-1/2}\left(\dfrac{a}{\varrho}\right)^2 & |\sigma| > a. \end{cases} \tag{2.3}$$

Here, a and A represent the sphere's radius and amplitude of oscillation, respectively. The variable ϑ denotes the azimuthal angle between the vertical and a point on the wave cone of the small-amplitude monochromatic internal waves. The notation $\nu = 0$ is included to emphasize that the kinematic viscosity, ν, is neglected in inviscid theories.

For simplicity, we have focused our attention on the cross-section through the upper wave beam, as shown in figure 1(*b*). The system's symmetry may ultimately be exploited to extend the results to the lower conical beam. Consistent with the schematic in figure 1(*b*), in (2.3) we have adopted the convention that the σ-axis is directed upward with $\sigma = 0$ corresponding to the centre of the wave beam.

In the far-field limit ($\varrho \gg a$), it is convenient to introduce an orthogonal, $\sigma - r$, coordinate system where r represents the along-beam distance, as illustrated in figure 1(*b*). Thus, we have $\varrho = \sqrt{r^2 + \sigma^2}$ and $\vartheta = \Theta - \tan^{-1}(\sigma/r)$. Equivalently, the along- and across-beam coordinates can be written in terms of cylindrical coordinates by

$$\sigma = -R\cos\Theta + z\sin\Theta, \quad r = R\sin\Theta + z\cos\Theta. \tag{2.4}$$

We note that far from the sphere, the inviscid theory predicts that the amplitude of the wave beam is negligibly small for $|\sigma| > a$. Within the conical wavefronts we have

$$\psi(r \gg a, |\sigma| < a)|_{\nu=0} \sim \mathrm{i}AaN\left(\frac{\cos^3\Theta}{\sin\Theta}\right)^{1/2}\left(\frac{a}{r}\right)^{1/2}\left[\frac{\sigma}{a} - \mathrm{i}\sqrt{1 - \left(\frac{\sigma}{a}\right)^2}\right]^{3/2}, \tag{2.5}$$

where, after taking the appropriate branch cut, we have used the identity $\exp[\mathrm{i}\cos^{-1}(x)] = x - \mathrm{i}(1 - x^2)^{1/2}$.

Equation (2.5) demonstrates that in the far field, the wave amplitude decreases approximately as $r^{-1/2}$, as expected for the radial energy flux to remain constant across any horizontal cross-section through the conical beam. Except for this radially dependent factor representing the expansion of the wave cone with height, the structure of the waves is determined entirely in terms of the across-beam coordinate σ.

2.2. *Viscous theory*

In adapting the result given by (2.5) to a viscous theory that accounts for the effects of attenuation of the wave beams, it is convenient to re-express the equation in terms of an integral formula. Using the formulae given by Gradshteyn & Ryzhik (1980, §6.671), we write

$$\psi(r \gg a, |\sigma| < a)|_{\nu=0} \sim \mathrm{i}AaN\left(\frac{\cos^3\Theta}{\sin\Theta}\right)^{1/2}\left(\frac{a}{r}\right)^{1/2}\left[\tfrac{3}{2}\mathrm{e}^{-\mathrm{i}3\pi/4}\int_0^\infty \frac{1}{k}J_{3/2}(ka)\mathrm{e}^{\mathrm{i}k\sigma}\,\mathrm{d}k\right]. \tag{2.6}$$

We exploit this σ-dependent integral in developing a theory for viscously attenuated wave beams. Following an approach similar to Hurley & Keady (1997), we assume the effects of viscosity are relatively small so that after multiplying by $r^{1/2}$ the dominant variations of the streamfunction occur in the across-beam direction.

Assuming the amplitude of the internal waves is small, by linearizing the Navier–Stokes and continuity equations in cylindrical coordinates, it can be shown that $\psi(R, z)$ satisfies

$$N^2 D_R^2\psi - \omega^2\tilde{\nabla}^2\psi + \mathrm{i}\omega\nu[\tilde{\nabla}^2\tilde{\nabla}^2\psi] = 0, \tag{2.7}$$

in which

$$D_R^2\psi \equiv \frac{\partial}{\partial R}\left(\frac{1}{R}\frac{\partial(R\psi)}{\partial R}\right)$$

and

$$\tilde{\nabla}^2 \equiv D_R^2 + \frac{\partial^2}{\partial z^2}.$$

In (2.7), ν is the kinematic viscosity. For salt water at room temperature and densities characteristic of laboratory experiments ($\rho \lesssim 1.05 \, \mathrm{g \, cm^{-3}}$), ν holds the approximately constant value of $0.01 \, \mathrm{cm^2 \, s^{-1}}$.

Analysis of (2.7) is facilitated by using (2.4) to transform from cylindrical coordinates to along- and across-beam coordinates.

We then define

$$\beta(r, \sigma) = \sqrt{\frac{r}{a}} \psi(r, \sigma).$$

This is substituted into (2.7) after applying the coordinate transformation (2.4). Using the boundary-layer approximation of Stevenson (1973), we assume along-beam changes are negligibly small compared with across-beam changes. For $r \gg \sigma$ and $r \gg a$, the leading-order terms of the resulting equation give

$$\frac{\partial^2 \beta}{\partial r \partial \sigma} - \frac{i\nu}{2N \sin \Theta} \frac{\partial^4 \beta}{\partial \sigma^4} = 0. \tag{2.8}$$

This equation for β is similar to that derived by Hurley & Keady (1997) for the streamfunction in their study of waves generated by an oscillating elliptical cylinder.

The solution of (2.8) is found by applying a Fourier transform in σ over non-negative wavenumber space. Explicitly, we find

$$\beta(r, \sigma) \sim \int_0^\infty F(K) \exp\left(-\lambda K^3 \frac{r}{a} + iK \frac{\sigma}{a}\right) dK, \tag{2.9}$$

where

$$\lambda = \frac{\nu}{2a^2 N \sin \Theta} \tag{2.10}$$

is a non-dimensional parameter which must be small for the boundary-layer approximation to be valid. Note that we have retained only those Fourier components with non-dimensional wavenumbers $K \geqslant 0$ because only these correspond to upward wave propagation (Lighthill 1978).

By analogy with the case of waves generated by an oscillating cylinder, we evaluate the result (2.9) in the limit $\nu \to 0^+$ and require a no-normal-flow boundary condition to determine $F(K)$. These steps are described explicitly in Appendix B. Thus we find, for $r \gg a$, the streamfunction is given by

$$\psi(r, \sigma) \sim \tfrac{1}{2} iAaN \cos \Theta \exp(-i\Theta) \sqrt{\frac{a}{r}} \int_0^\infty \frac{1}{K} J_{3/2}(K) \exp\left(-dK^3 + iK \frac{\sigma}{a}\right) dK. \tag{2.11}$$

Here, using (2.10), we have defined the non-dimensional along-beam distance d by

$$d \equiv \lambda r / a = \frac{\nu r}{2a^3 N \sin \Theta}. \tag{2.12}$$

This parameter is significant in that it can be used to establish the distance over which viscous effects become important.

The formula given by (2.11) in the inviscid limit is different in magnitude from (2.5) by a factor $(\tan \Theta)^{1/2}$. The discrepancy is due to the boundary-layer approximation, which is used to enforce no-normal-flow boundary conditions and which neglects the dependence of r upon ϱ near the sphere (see Appendix B). For example, in experiments with $\Theta \simeq 60°$, (2.11) predicts 32% larger wave amplitudes than (2.5). As shown in §4.3, (2.11) better represents the observed collapse of data.

The result given by (2.11) is remarkably similar to that of Hurley & Keady (1997) for the oscillating circular cylinder. Employing the corresponding coordinate system

to that used here for the oscillating sphere (e.g. see Sutherland *et al.* 1999) the stream-function in the first quadrant is given by

$$\psi_{\text{cyl}}(r, \sigma) \sim \tfrac{1}{2}iAaN \cos \Theta \exp(-i\Theta) \int_0^\infty \frac{1}{K} J_1(K) \exp\left(-dK^3 + iK\frac{\sigma}{a}\right) dK, \quad (2.13)$$

where d is again given by (2.12).

Other than the conical expansion factor $(a/r)^{1/2}$, the only difference between the far-field formulae for waves generated by a sphere and cylinder is the order of the Bessel function in the integrand.

2.3. *Theoretical results*

For internal waves visualized in experiments by schlieren techniques, the images result due to changes in the density gradients, which result from waves that compress and stretch the distance between isopycnal surfaces. Thus, for direct comparison with experimental results, we calculate the theoretical amplitude of both the change in the perturbation squared buoyancy frequency, ΔN^2, and its time derivative, N_t^2. These fields, which are proportional to the perturbation density gradient, are used because they can be compared easily with the background buoyancy frequency and thus provide an intuitive measure of the relative amplitude of the waves.

Explicitly, using linear theory,

$$\Delta N^2 \equiv \frac{-g}{\rho_0} \frac{\partial \rho}{\partial z} \sim iN \sin \Theta \frac{\partial^2 \psi}{\partial \sigma^2}. \quad (2.14)$$

Using (2.11), we find

$$\Delta N^2 \sim A_{N^2} \exp(-i\Theta) \sqrt{\frac{a}{r}} \int_0^\infty K J_{3/2}(K) \exp\left(-dK^3 + iK\frac{\sigma}{a}\right) dK, \quad (2.15)$$

where

$$A_{N^2} = \frac{1}{2} \frac{A}{a} N^2 \sin \Theta \cos \Theta. \quad (2.16)$$

Similarly,

$$N_t^2 \equiv -i\omega \left(\frac{-g}{\rho_0} \frac{\partial \rho}{\partial z}\right) \sim N^2 \sin \Theta \cos \Theta \frac{\partial^2 \psi}{\partial \sigma^2}. \quad (2.17)$$

Hence,

$$N_t^2 \sim -iN \cos \Theta A_{N^2} \exp(-i\Theta) \sqrt{\frac{a}{r}} \int_0^\infty K J_{3/2}(K) \exp\left(-dK^3 + iK\frac{\sigma}{a}\right) dK. \quad (2.18)$$

We use a fast Fourier transform algorithm (Press *et al.* 1993) to evaluate these integrals numerically. Care is taken to ensure that the domain size is sufficiently large and resolution sufficiently high that convergence is attained to less than 0.1% accuracy.

Figure 2 shows across-beam plots at two different positions along the beam of the normalized ΔN^2 field, $\Delta N^2/A_{N^2}$. The curves are calculated using parameters similar to some of the experiments with the small sphere. Explicitly, we set $a = 1.9$ cm, $\omega = 0.5 \text{ s}^{-1}$, $N = 1.0 \text{ s}^{-1}$ and $\nu = 0.01 \text{ cm}^2 \text{ s}^{-1}$. Thus, $\Theta \simeq 60°$. Both plots show the amplitude envelope as well as the instantaneous amplitude profile at four different phases of its motion. Note that the wave crests move to decreasing σ with increasing phase. This is consistent with the downward motion of phase lines expected for upward propagating waves.
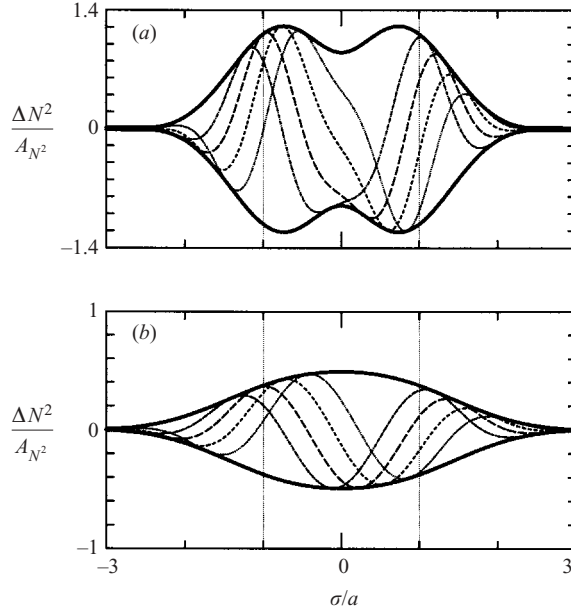
FIGURE 2. Across-beam plots of $\Delta N^2/A_{N^2}$ at (*a*) $r/a = 5$ (*d* = 0.008) and (*b*) $r/a = 15$ (*d* = 0.024). In each case, the thick solid lines denote the envelope of the waves. The specific structure of the waves is also shown at the following phases: $\phi = 0$ (dotted line), $\pi/4$ (short-dashed line), $\pi/2$ (long-dashed line), $3\pi/4$ (dash-dotted line).

A striking difference between the two plots is the structure of the amplitude envelope which exhibits two peaks near $\sigma = \pm a$ for $r/a = 5$ (figure 2*a*), but only one peak at $\sigma = 0$ for $r/a = 15$ (figure 2*b*). These plots therefore illustrate the transition of the wave-beam structure from bimodal to unimodal. The transition occurs because of the broadening of the beams under the effects of viscous attenuation.

The transition from bimodal to unimodal structure is better illustrated in figure 3 which shows along-beam cross-sections of the normalized streamfunction and ΔN^2 fields. The curves are computed using the same parameters as those used to compute the curves in figure 2. Cross-sections are shown along the beam centreline, where $\sigma = 0$, and along $\sigma = a$. The latter is chosen since inviscid theory predicts large along-beam velocities along this cross-section, which is tangential to the sphere.

Along both the $\sigma = 0$ and $\sigma = a$ cross-sections shown in figure 3(*a*), the streamfunction amplitude decreases monotonically primarily owing to the wave-cone expansion factor $r^{-1/2}$, but also in part owing to viscous attenuation. For all r, the streamfunction amplitude, which is normalized by $A_\psi = ANa \cos \Theta/2$, is largest along the centreline of the wave beam, where $\sigma = 0$.

In contrast, figure 3(*b*) shows that for $r/a \lesssim 6.8$ ($d \lesssim 0.011$) the amplitude of the ΔN^2 field is larger at $\sigma = a$ than at $\sigma = 0$. This is consistent with the structure of bimodal wave-beams. Thus, the ΔN^2 field (and hence schlieren visualization methods) more clearly illustrates the bimodal to unimodal transition.

This is not to say that the streamfunction field is unimodal. As illustrated below, if we define bimodal waves as those with positive curvature to the amplitude envelope at $\sigma = 0$ and unimodal waves as those with negative curvature at $\sigma = 0$, then both the streamfunction and ΔN^2 field show a bimodal to unimodal transition. For sufficiently
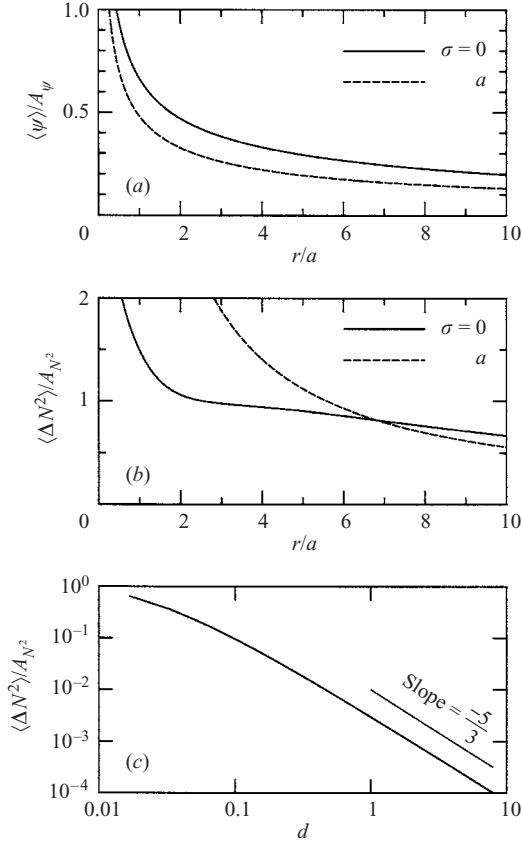
FIGURE 3. Along-beam plots of (*a*) the normalized streamfunction envelope, $\langle\psi\rangle/A_\psi$, (*b*) $\langle\Delta N^2\rangle/A_{N^2}$ near the source plotted as a function of r/a and (*c*) the far-field values of $\langle\Delta N^2\rangle/A_{N^2}$ as a function of $d = \lambda r/a$ and shown as a log–log plot. In (*a*) and (*b*) solid and dotted lines show cross-sections along $\sigma = 0$ and a, respectively. In (*c*) only the cross-section along $\sigma = 0$ is shown. The thin solid line in (*c*) shows the predicted slope of the curve in the asymptotic regime.

small r where the streamfunction is bimodal, the peak amplitude occurs between $\sigma = 0$ and $\sigma = a$.

2.4. *Bimodal to unimodal beam transition*

The explicit integral formula for the wave beams permits us to determine at what position along the beams their structure changes from bimodal to unimodal. The location itself is ambiguous depending upon the basic state field being analysed and upon the mathematical definition of the transition.

The distinguishing characteristic between bimodal and unimodal wave beams is that the curvature of the amplitude envelope of the former is positive along the centreline (where $\sigma = 0$) whereas it is negative for the latter.

The non-dimensional distance $d = d_c$ at which this occurs for the streamfunction, for example, is therefore given implicitly by

$$\left(\left[\frac{\partial^2}{\partial\sigma^2}\langle\psi\rangle\right]\bigg|_{\sigma=0}\right)\bigg|_{d=d_c} = 0. \tag{2.19}$$

Here, $\langle\psi\rangle$ represents the amplitude envelope of the streamfunction.

Field	Cylinder ($\mu = 1$)	Sphere ($\mu = 3/2$)
Streamfunction	$d_\star = 0.00812$ $d_c = 0.00605$ $p_\nu = 1/3$	$d_\star = $ (none) $d_c = 0.00507$ $p_\nu = 1$
Velocity, displacement	$d_\star = 0.01463$ $d_c = 0.01650$ $p_\nu = 2/3$	$d_\star = 0.00861$ $d_c = 0.01086$ $p_\nu = 4/3$
$\Delta N^2, N_t^2$	$d_\star = 0.02071$ $d_c = 0.02552$ $p_\nu = 1$	$d_\star = 0.01254$ $d_c = 0.01644$ $p_\nu = 5/3$

TABLE 1. Theoretically predicted values of the non-dimensional along-beam distance at which the centreline of the envelope is a maximum ($d_\star$) and where the across-beam curvature is zero along the centreline (d_c). Also listed are power law decay rates ($\propto r^{-p_\nu}$) of centreline beam amplitudes as $d \to \infty$.

Defining

$$I(d; p, \mu) = \int_0^\infty K^{p-1} J_\mu(K) \exp(-K^3 d)\, dK, \qquad (2.20)$$

it is a simple matter to show that (2.19) together with (2.11) leads to the condition that d_c must satisfy $I^2(d_c; 1, 3/2) = I(d_c; 0, 3/2) I(d_c; 2, 3/2)$.

Likewise, because along-beam derivatives are negligibly small compared with across-beam derivatives, the transition distance for the velocity field and vertical displacement fields are determined by the condition that the curvature of $\langle \partial \psi / \partial \sigma \rangle$ is zero along the centreline of the beam at some critical distance d_c. This amounts to finding the value of d_c that satisfies $I^2(d_c; 2, 3/2) = I(d_c; 1, 3/2) I(d_c; 3, 3/2)$.

For comparison with schlieren experiments, it is useful to evaluate the zero-curvature condition for $\langle \Delta N^2 \rangle \propto \langle \partial^2 \psi / \partial \sigma^2 \rangle$, because this field is proportional to the density gradient field, which is directly measured. For this field, d_c satisfies $I^2(d_c; 3, 3/2) = I(d_c; 2, 3/2) I(d_c; 4, 3/2)$.

Values of d_c are evaluated numerically and are given in table 1. For convenience, the table also gives corresponding values of d_c predicted for an oscillating circular cylinder. These values are found by evaluating the corresponding integral conditions, but for Bessel functions of order $\mu = 1$ instead of $3/2$ in the integrand.

The transition distance for all three fields is smaller for the sphere than for the cylinder. For both the sphere and the cylinder, the transition distance is largest for the ΔN^2 field.

Although d_c provides a useful mathematical definition in terms of the curvature, other measures of the transition distance are also practical for the purpose of comparison with observations. One possibility is to define the transition as occurring where the amplitude of the beam along the centreline exceeds the amplitude at $\sigma = a$. For example, figure 3(b) shows that this occurs for the ΔN^2 field at $r/a = 6.8$, corresponding to $d \simeq 0.011$. This value is approximately two-thirds of the transition distance d_c.

The peaks on either flank of the centreline of the bimodal wave-beam broaden owing to viscous attenuation and this acts both to decrease the amplitude of the peaks and to increase the amplitude of the beam along the centreline. Thus, near the sphere the amplitude of the waves should decrease less quickly than $r^{-1/2}$. After the beams

have merged, the centreline amplitude should decrease faster than $r^{-1/2}$ owing to the combined effects of the expanding wave cone and viscosity.

This leads us to define the transition distance $d_\star$ where, after multiplying by $(r/a)^{1/2}$, the amplitude along the centreline of the beam is predicted to be greatest. Corresponding to the streamfunction of the wave cone emanating from an oscillating sphere, this is given by

$$\left(\left[\frac{\partial}{\partial r} \langle \beta \rangle \right] \bigg|_{\sigma=0} \right) \bigg|_{d=d_\star} = 0. \tag{2.21}$$

This implicit condition on $d_\star$ simplifies to $I(d_\star; 3, 3/2) = 0$.

Corresponding transition distances for the velocity and ΔN^2 fields generated by an oscillating sphere can be found. Likewise, these are determined for an oscillating circular cylinder, although in this case it is not necessary to correct for the wave-cone expansion factor by multiplying by $(r/a)^{1/2}$.

Values of $d_\star$, given in table 1, are typically smaller than d_c with the exception of its value for the streamfunction. In this case, for the cylinder, it is greater than d_c and for the sphere, no maximum of β occurs within the wave field.

2.5. *Asymptotics*

In an analysis similar to that of Sutherland & Linden (2002) for the oscillating cylinder, we can compute for the oscillating sphere asymptotic formulae for the decreasing amplitude of the wave beam in the far field. Thus, we can evaluate the relative importance of the decrease in amplitude of the wave beam due to the expansion of the wave cone as well as viscous attenuation.

From (2.11), the streamfunction along the centreline of the upward-propagating wave cone is

$$\psi|_{\sigma=0} \propto \sqrt{\frac{a}{r}} \int_0^\infty \frac{J_{3/2}(K)}{K} \exp(-K^3 d) \, \mathrm{d}K. \tag{2.22}$$

Through differentiation of (2.11) with respect to σ, the asymptotic behaviour of dynamical fields of interest can be deduced. For convenience, we define

$$f(d; p) = \int_0^\infty J_{3/2}(K) K^{p-1} \exp(-K^3 d) \, \mathrm{d}K. \tag{2.23}$$

Then, for large d, the along-beam velocity is proportional to $f(d, 1)$ and $N_t^2|_{\sigma=0} \propto f(d, 2)$.

Standard asymptotic analyses (i.e. Watson's Lemma, see Bender & Orszag 1999) give

$$f(d; p) \sim \frac{1}{3 \times 2^{3/2}} d^{-(p+3/2)/3} \sum_{n=0}^\infty \frac{(-1)^n \Gamma\left(\dfrac{p + 2n + 3/2}{3}\right)}{2^{2n} \, n! \, \Gamma(n + 5/2)} d^{-2n/3} \tag{2.24}$$

Therefore, to leading order, the far-field streamfunction is predicted to decrease as $r^{-1/2} d^{-1/2} \propto r^{-1}$. That is, the effects of viscous attenuation are as important as the expansion of the wave cone in determining the resulting decrease of the amplitude. Viscous attenuation effects are more significant for the velocity, ΔN^2 and N_t^2 fields. Explicitly, the velocity, which is proportional to $\partial\psi/\partial\sigma$, is predicted to decrease as $r^{-1/2} d^{-5/6} \propto r^{-4/3}$. The ΔN^2 and N_t^2 fields are predicted to decrease as $r^{-1/2} d^{-7/6} \propto r^{-5/3}$.

For both the oscillating cylinder and sphere, the amplitude of the wave beam in the far field decreases according to the power law r^{-p_v}. Values of the power law exponent, p_v, are given in table 1.

Figure 3(c) shows a log–log plot of ΔN^2 *vs.* d and, for $d > 1$, compares its slope to that predicted by asymptotic analysis. The plot demonstrates that the asymptotic approximation is indeed accurate even for small values of d. The slope of the curve lies within 10% of its asymptotic value for $d \gtrsim 0.25$.

In most experimental investigations of oscillating cylinders and spheres (Mowbray & Rarity 1967b; Stevenson 1969; Sutherland *et al.* 1999) including those presented here, even this small value of d is too large to be accessible. For example, with $a = 1.9$ cm, $N = 1.0 \, \text{s}^{-1}$ and $\Theta = 60°$, $d = 0.25$ corresponds to $r = 297$ cm. To investigate the evolution of waves over this distance would require a prohibitively large tank.

We therefore confine ourselves to examining the behaviour of the waves near the oscillating sphere and to studying, in particular, the transition from bimodal to unimodal waves.

3. Experimental methods

3.1. *Experimental set-up*

The experiments performed in this study are similar in scope and design to those described by Sutherland *et al.* (1999). They are performed in a Perspex tank having a height $H = 48.6$ cm, length $L_0 = 47.6$ cm and width, $L_t = 47.7$ cm. The tank is filled to a depth of 44.3 cm with a uniformly stratified salt solution using a 'double bucket' system (Oster 1965). A traversing conductivity probe is used to measure density as a function of depth. In the experiments reported upon here, the measured buoyancy frequency, determined from the slope of the best fit line through the density profile, ranges between $N = 0.94$ and $1.00 \, \text{s}^{-1}$ with a measurement error of $0.02 \, \text{s}^{-1}$.

Two hollow plastic spheres of radii $a = 1.9$ and 3.2 cm are employed in this study. Both spheres are filled with a salt water solution so that they are almost neutrally buoyant when suspended underwater.

As shown in figure 4, each sphere is attached to a thin metal rod. Its diameter is 2.5 mm for the large sphere and 1.7 mm for the small sphere. The other end of the rod is connected through a hinge to a sinusoidally oscillating arm. In each case, the rod is passed through a narrow guide placed across the top of the tank thus ensuring that the sphere's motion is vertical. A 'reflection-barrier' is positioned above and to the left of the sphere in the tank. This acts to prevent interference from reflected waves on the left-hand side of the upward propagating wave cone.

The frequency of oscillation is controlled by adjusting the rate of rotation of the motor. In the experiments reported upon here, the oscillation frequency ranges from $\omega = 0.287$ to $0.819 \, \text{s}^{-1}$. Thus, as predicted by linear theory, wave cones are generated forming angles to the vertical of $\Theta = \cos^{-1}(\omega/N)$ ranging between 30.9° and 72.4°. Values of ω closer to either 0 or N were not examined in order to minimize the interference between the upper and lower wave cones and between the right- and left-hand sides of the wave cones. Thus, we are able to compare the experimental results directly with theory for a single wave cone.

In order to investigate the range of validity of linear theory, we examine wave generation by spheres oscillating at different amplitudes. The amplitude of oscillation is controlled by altering L_A, the distance between the arm's pivot point and the position of the hinge, as shown in figure 4(a). Here, we examine waves generated by the large sphere oscillating with relative amplitudes of $A/a = 0.10$, 0.18 and 0.27, and
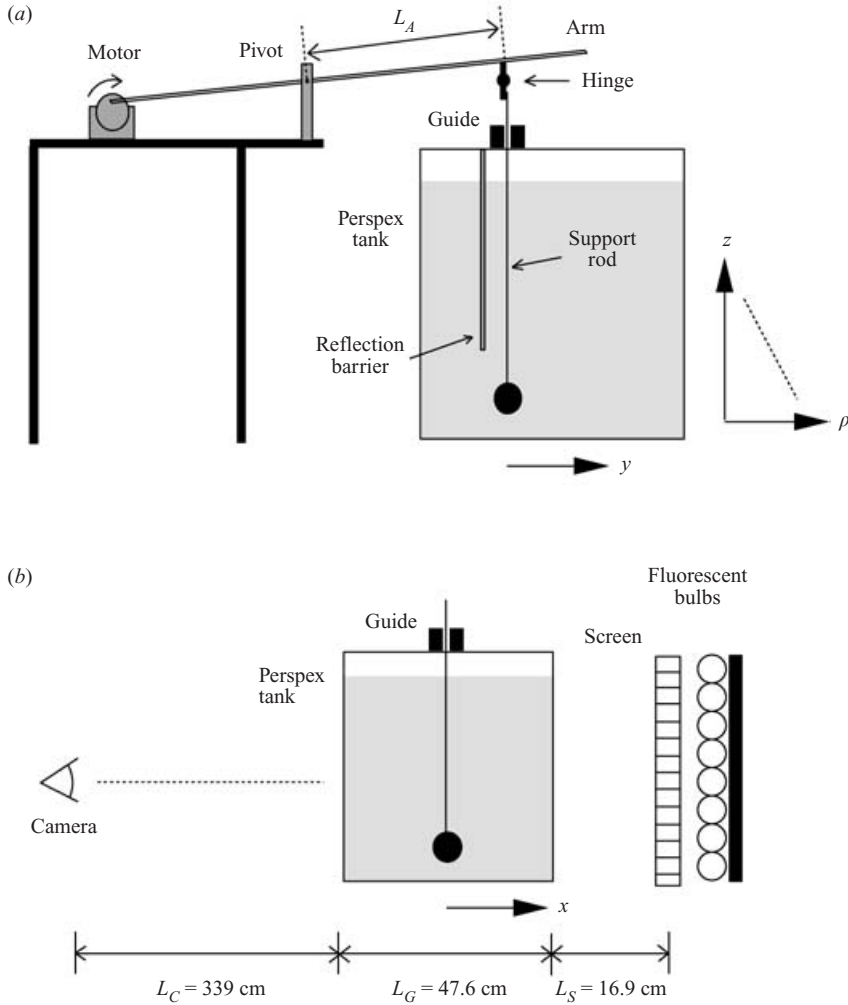
FIGURE 4. (*a*) Front view of the tank showing the oscillating sphere mechanism. (*b*) Side view of the tank showing the relative position of the tank to the CCD camera. (Figure not to scale.)

by the small sphere oscillating with relative amplitudes of $A/a = 0.15$, 0.19 and 0.26. Even for runs with the largest amplitude of oscillation, the flow around the sphere is observed to be laminar.

3.2. *Qualitative schlieren visualization*

The internal wave field is visualized by employing a 'synthetic schlieren' system. The implementation of the system and the measurement of line displacements are described in detail by Sutherland *et al.* (1999). Only the relevant features are summarized here.

As with all schlieren systems, synthetic schlieren visualiszes internal waves by enhancing the way light is deflected through a stratified fluid. Because the index of refraction is proportional to salinity (Weast 1981), light rays are deflected to a greater extent if they pass through larger density gradients. Thus, the light rays are deflected upwards and downwards as internal waves compress and stretch, respectively, isopycnal surfaces. Synthetic schlieren visualizes these deflections by digitally recording distortions of an image placed behind the tank.

The set-up of synthetic schlieren is shown in figure 4(*b*). In the set-up, a translucent screen of evenly spaced 0.25 cm thick horizontal black lines is placed a distance $L_s = 16.9$ cm behind the tank. The screen is illuminated from behind by a rack of fluorescent bulbs. The experiment is recorded on digital tape by a CCD camera positioned approximately $L_c = 339$ cm in front of the tank. In order to capture as much of one quadrant of the wave cone as possible, the sphere is positioned toward the tank's lower left-hand corner.

The camera is itself connected to a computer running DigImage (Dalziel 1992), which is used to enhance and analyse images from the camera. Typically, the area of one pixel in an image is 0.05×0.05 cm^2.

An illustration of the visualization technique is shown in figures 5. Figure 5(*a*) shows a snapshot taken by the camera after the large sphere has undergone two large-amplitude ($A/a = 0.27$) oscillations. Part of the sphere (in black) is shown in the bottom left-hand corner of the image. The rest of the frame is dominated by horizontal lines, which is the image of the screen behind the tank. Though it cannot be seen by eye, the image of the lines is distorted owing to the presence of waves in the tank. By subtracting this image from one taken before the experiment began, the distortion can be enhanced. This is illustrated in figure 5(*b*), which clearly shows a wave-beam emanating upward and to the right of the sphere.

Through interpolation of the changing intensities of adjacent pixels in the image, the apparent vertical displacement, Δz, of the lines in the image can be measured with an accuracy as small as 0.002 cm. Performing this calculation for pixels corresponding to the edges of the dark lines on the screen, and using a Gaussian weighted average of the results to determine the displacements of the remaining pixels, we obtain, after filtering, a matrix of data $\Delta z(y, z)$. This is represented, for example, in figure 5(*c*), which shows the apparent displacement of lines computed from the image in figure 5(*a*). Note that the lines in this experiment are displaced by no more than 0.02 cm, explaining why such displacements are hard to detect by eye.

Figure 5(*c*) also illustrates a useful advantage of schlieren, as opposed to *in situ* probe measurements, for measuring wave amplitudes. Theory predicts that the amplitude of the waves should decrease approximately as $r^{-1/2}$. However, the image shows that the value of Δz remains large far from the sphere. This occurs because the wave cone disturbs the stratified fluid over a wider distance far from the cone. Even though the amplitude is less, the light ray passes through a longer disturbance, and cumulatively this acts to maintain a strong signal even far from the source.

Another important advantage of synthetic schlieren over other schlieren systems is that it can be used to measure two-dimensional (planar) and axisymmetric wave amplitudes from a single field of view. In the former case (used, for example, to measure internal waves generated by an oscillating cylinder (Sutherland *et al.* 1999; Sutherland & Linden 2002)), it is a straightforward matter to relate the apparent image displacement Δz to the ΔN^2 field, which in turn is proportional to the change in the density gradient due to waves.

The computation is more complicated for the axisymmetric waves generated by an oscillating sphere. It requires the use of tomographic inversion techniques to determine $\Delta N^2(R, z)$ from $\Delta z(y, z)$, a procedure discussed in detail by Onu, Flynn & Sutherland (2003) and described briefly below.

3.3. *Axisymmetric schlieren measurements*

In order to relate ΔN^2 to Δz, we first determine how a light ray is bent owing to variations in the index of refraction, $n(x, z)$. Because we use an image of horizontal
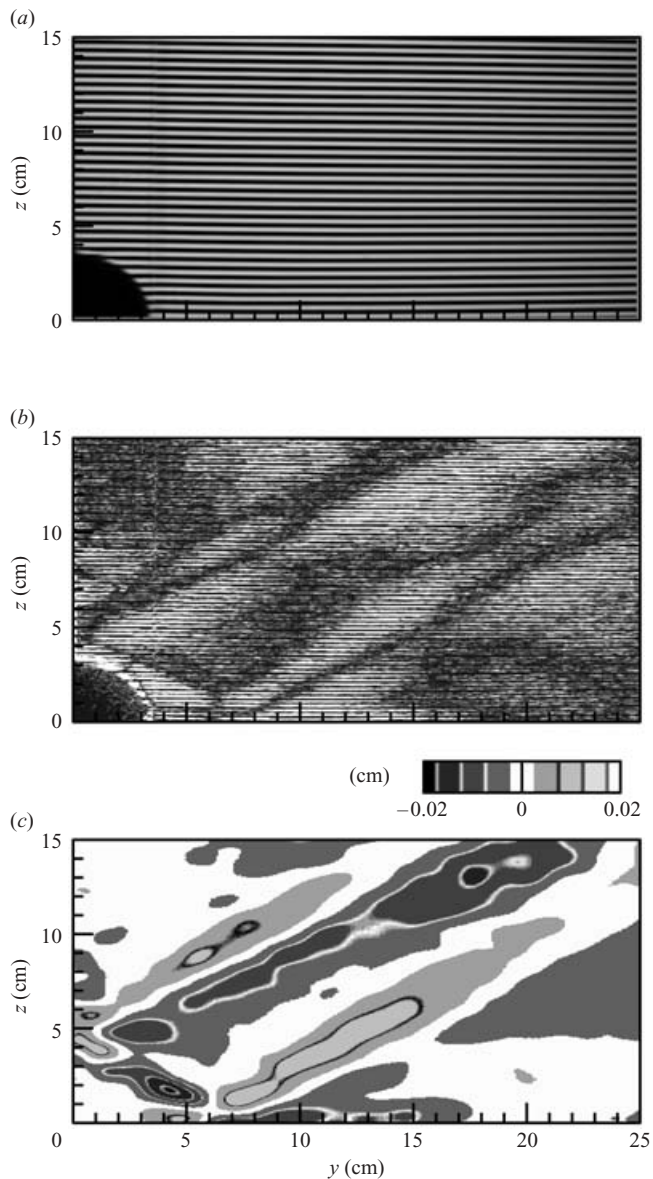
FIGURE 5. (*a*) Snapshot of the experiment taken at the beginning of the third oscillation, (*b*) synthetic schlieren image determined from that shown in (*a*), and (*c*) the apparent vertical displacement, Δz, of lines in the image computed from the image shown in (*a*).

lines, we ignore variations of n in the y-direction as deflections in the along-tank direction are not measured.

Using Snell's Law under the approximation that the light rays pass almost horizontally through the tank, the vertical rise $z(x)$ as the light ray passes through the tank in the x-direction is given by the differential equation

$$z'' \left(z' \frac{1}{\partial n/\partial x} + \frac{1}{\partial n/\partial z} \right) = \frac{1}{n}, \tag{3.1}$$

in which primes denote derivatives with respect to x.

Because the light ray traverses only a small vertical distance (typically less than $1\,\text{cm}$) as it passes through the tank, we further assume that n depends only linearly on z. Explicitly,

$$n(x, z) = \alpha_0(x) + \alpha_1(x)z. \tag{3.2}$$

Substituting this into (3.1) and estimating characteristic scales of α_0 and α_1, we can use perturbation theory to find an approximate solution to the differential equation:

$$z(x) = z_i + x \cot \phi_i - \gamma \int_0^x \int_0^{\hat{x}} N^2(X)\,\mathrm{d}X\,\mathrm{d}\hat{x}. \tag{3.3}$$

Here, z_i is the initial height and ϕ_i the initial angle of the ray as it enters the stratified fluid. For salt water, the physical constant γ is given by

$$\gamma = \frac{1}{g} \frac{\rho_0}{n_0} \frac{\Delta n}{\Delta \rho} \simeq 1.878 \times 10^{-4}\,\text{s}^2\,\text{cm}^{-1}.$$

By repeatedly applying Snell's law as the ray travels from the camera to the grid of lines, the height at the image of a light ray that meets the camera at height z_0 and with (small) angle ϕ_0 to the horizontal can be found. Finally, the displacement of the light ray, Δz, can be determined as a function of the change in the squared buoyancy frequency. Explicitly, we have

$$\Delta z = -\gamma n_w \left\{ L_s \frac{n_w}{n_a} \int_0^{L_t} \Delta N^2(x)\,\mathrm{d}x + \int_0^{L_t} \int_0^x \Delta N^2(\hat{x})\,\mathrm{d}\hat{x}\,\mathrm{d}x \right\}. \tag{3.4}$$

In the special case in which N is independent of x, this equation corresponds to that derived by Sutherland et al. (1999) in their study of waves generated by an oscillating cylinder. Their result is straightforward to invert. That is, we can write an explicit algebraic formula for the field $\Delta N^2(y, z)$ in terms of $\Delta z(y, z)$.

For axisymmetric waves, ΔN^2 is a function of z and the radial distance, R, from the z-axis. Hence, it is necessary to discretize the formula given by (3.4) and numerically invert the resulting matrix equation.

In practice, at each vertical level, z_s, we represent $\Delta N^2(R; z_s)$ by an $N = 512$-component vector, $(\Delta N^2(R_1; z_s), \ldots, \Delta N^2(R_N; z_s))$ where R_i represents the mean radius of the ith ring. The vector size is determined by the number of horizontal pixels in the original digitized image of the experiment. The matrix inversion is performed numerically using the LU decomposition routines described in §2.3 of Press et al. (1993). The inversion routine is repeated for each row of data at 480 different vertical levels z_s. Thus, the $\Delta N^2(R, z)$ field is reconstructed from the $\Delta z(x, z)$ data. The calculation is performed on a single processor of an SGI Origin 2000 with $195\,\text{MHz}$ R10K CPUs. The processing of a single 512×480 array takes less than $10\,\text{min}$.

4. Results

4.1. Wave structure

Figure 6 shows the structure and amplitude of upward propagating internal waves generated by the small sphere. Figure 6(a), which plots contours of the ΔN^2 field, clearly shows a wave beam emanating from the sphere at an angle $\Theta \simeq 61°$ to the vertical, the angle predicted by linear theory. Analyses of the N_t^2 field, not shown here, give similar results.

Though the signal noise of the corresponding Δz field is relatively small, we find that tomographic inversion acts to magnify these errors. In figure 6(a), the noise is
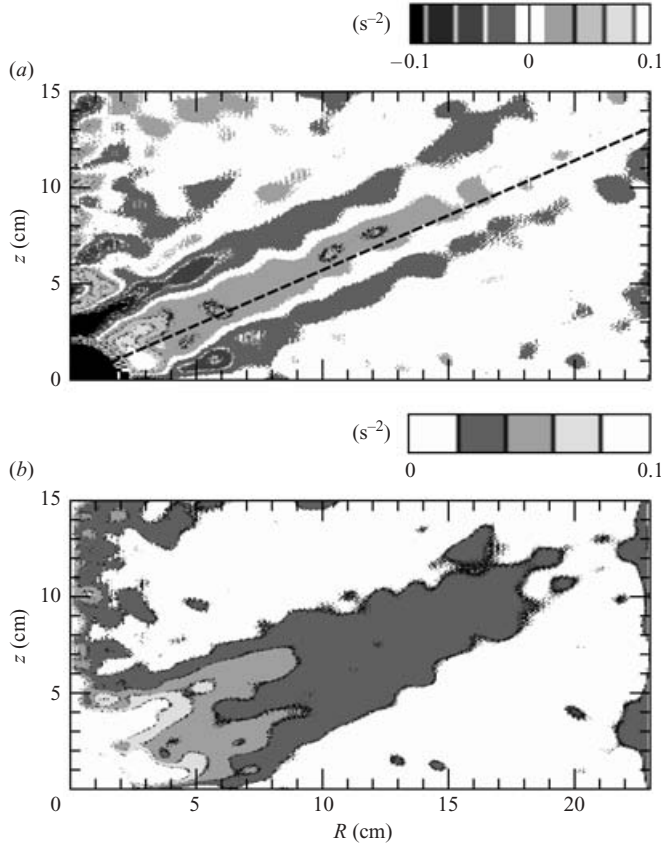
FIGURE 6. (*a*) The ΔN^2 field computed from an experiment with the small sphere oscillating with relative frequency $\omega/N = 0.49$ and relative amplitude $A/a = 0.26$. The field is evaluated at the phase $\phi = 0$, as the sphere moves downward through its equilibrium position. The diagonal dashed line is the line passing through the centre of the sphere at an angle $\Theta = \cos^{-1}(\omega/N) \simeq 61°$ to the vertical. (*b*) Shows the amplitude envelope, $\langle \Delta N^2 \rangle$, of the ΔN^2 field.

pronounced near the right and left margins of the image. Fortunately, the signal from the wave beam is stronger than the errors, particularly over the middle of the domain. Along the beam, the noise results in variations of the order of $0.01\,\mathrm{s}^{-2}$, or 1% of the background density gradient. Near the sphere, the signal from the waves is typically an order of magnitude larger than the noise.

To reduce further the effect of signal noise and also to examine the bimodal to unimodal transition, we calculate the amplitude envelope of the ΔN^2 field: $\langle \Delta N^2 \rangle$. This is done by computing the ΔN^2 field at sixteen different times during one period of oscillation. Explicitly, the field is computed at phases $\phi = 0, \pi/8, \ldots, 15\pi/8$, with $\phi = 0$ corresponding to the sphere moving downward through its equilibrium position. We then compute the root-mean-square average of the sixteen fields and multiply the result by $2^{1/2}$.

In order to ensure that waves reflecting off the tank boundaries interfere negligibly, we compute this average from images taken between the second and third oscillations of the sphere. Linear theory predicts that at $\Theta = 60°$, energy is transported at the group velocity between only $3.5a$ and $5.2a$ from the sphere during this time interval.
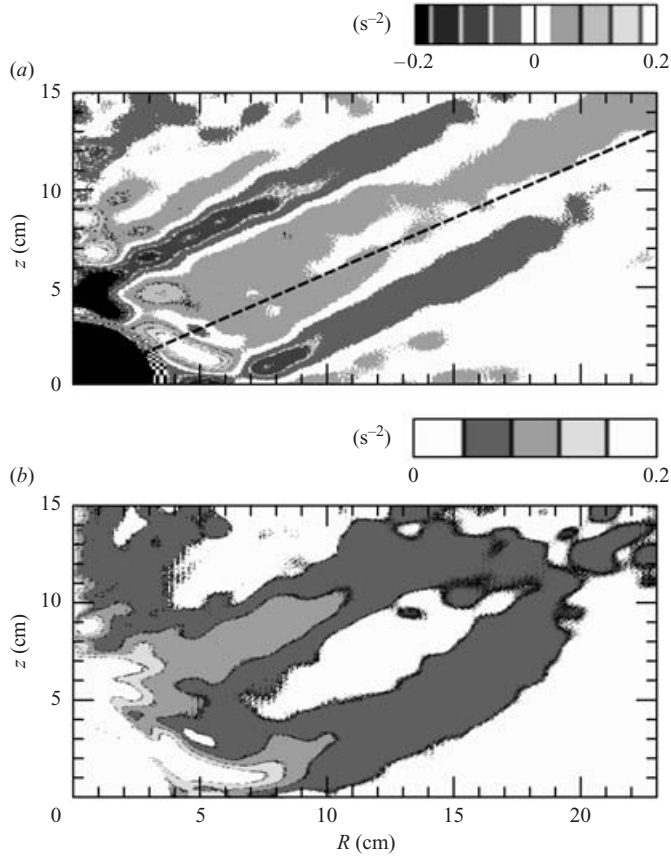
FIGURE 7. As in figure 6, but determined from an experiment with the large sphere oscillating with relative amplitude $A/a = 0.27$.

Our analysis reveals, however, that a quasi-steady state is established to within experimental noise over the field of view extending to $8a$ and $14a$ for the large and small sphere experiments, respectively. This is confirmed by subtracting the Δz fields taken at $\phi = 0$ for the second and third oscillation periods and dividing the result by the root-mean-square average. Thus, we conclude that the initial transient waves and the waves reflected from the tank boundaries have negligibly small influence upon the waves measured in the field of view of the experiment.

Figure 6(b) shows the amplitude envelope computed in this way between the second and third oscillations of the sphere. The image clearly shows that the amplitude of the waves near the sphere is largest on either flank of the centreline, but far from the sphere the amplitude is largest along the centreline. The image also shows the rapid decrease in amplitude of the wave beam with distance from the sphere.

These results are compared with those measured in an experiment employing the large sphere in figure 7. The ΔN^2 field shown in figure 7(a) is computed from the Δz field shown in figure 5. Because the amplitude of oscillation is larger, the signal from the wave beam is stronger and can be visualized over noise farther from the sphere.

In experiments with both the small and large sphere, we observe the transition from bimodal to unimodal waves with distance from the source. As expected, the
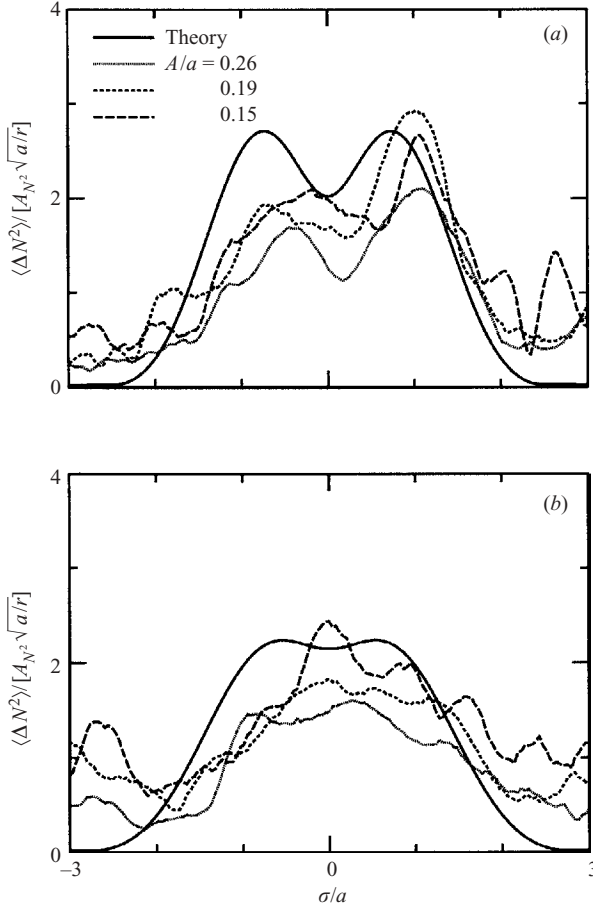
FIGURE 8. Across beam plots at (*a*) $r/a = 5$ ($d = 0.00801$) and (*b*) $r/a = 8$ ($d = 0.01282$) of the normalized $\langle \Delta N^2 \rangle$ field determined from experiments with the small sphere oscillating at three amplitudes (dotted, small-dashed and long-dashed curves, as indicated). The results are compared with theory (solid line).

amplitude envelope generated in large-sphere experiments exhibits bimodal behaviour farther from the sphere because the distance between the two tangents at $\sigma = \pm a$ is greater.

4.2. *Amplitude dependence*

We compare theoretical predictions derived from the streamfunction given by (2.11) to experimental results by taking across-beam and along-beam cross-sections through the amplitude envelope data and we plot the re-scaled results against suitable non-dimensional parameters.

Figures 8 and 9 compare the results of three experiments in which the small sphere oscillates at different amplitudes, but at fixed relative frequency $\omega/N \simeq 0.49$. Figure 8 shows across-beam cross-sections normalized by $A_{N^2}(a/r)^{1/2}$ where A_{N^2}, given by (2.16), is proportional to the amplitude of oscillation, A. Consistent with linear theory, the normalized curves from the three experiments approximately overlap. The relative amplitude of the wave beam in experiments with $A/a = 0.26$ is generally
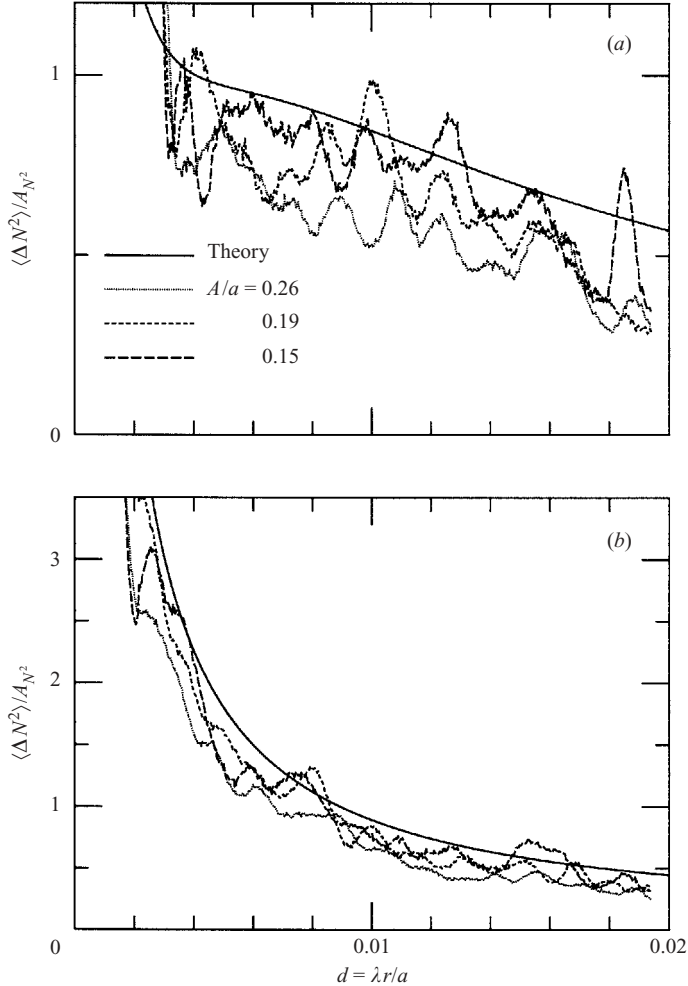
FIGURE 9. Comparison between the theoretical and experimental profiles of the $\langle \Delta N^2 \rangle / A_{N^2}$ field along the slice (a) $\sigma = 0$ and (b) $\sigma = a$ for small-sphere experiments.

smaller than the relative amplitude of the waves in the two experiments with smaller A/a. However, it is difficult to argue that this is a real effect because of the high background noise level.

At $r/a = 5$, all three experimental curves exhibit a pronounced peak near $\sigma = a$. This is consistent with theory which predicts that the wave beam is bimodal for $d \simeq 0.008 < d_c \simeq 0.016$.

All three experiments reveal an asymmetric structure at $r/a = 5$: there is no pronounced peak near $\sigma = -a$. As shown below, the large-sphere experiments do not exhibit such asymmetry. In light of these results, there are three reasons why the small-sphere wave beams could exhibit this asymmetric structure, though only one explanation turns out to be reasonable. We might expect the asymmetry results from destructive interference with the upward and downward propagating wave cones. Because the bottom flank of the wave beam on the upper cone interacts more strongly with the lower cone than its top flank, a relative reduction in amplitude should result. However, at $r/a = 5$, the distance between the point $\sigma = -a$ and the

mid-point between the two wave cones is approximately $1.6a$. This is sufficiently far away that destructive interference should be negligibly small. For example, in theory, the amplitude envelope at $\sigma/a = 3$ is less than 1% of the peak value of $\langle \Delta N^2 \rangle$ at $r/a = 5$.

A second possible reason for the asymmetry is that the approximation $\varrho \simeq r$ is inaccurate near the sphere. However, even at $r/a = 5$, this turns out to be a good approximation: the factor $(a/\varrho)^{1/2}$ differs from $(a/r)^{1/2}$ by less than 1% at $\sigma/a = \pm 1$. We might argue that a more accurately derived theory, which accounts for the variation in ϱ with r near the sphere, would predict asymmetric structure far from the sphere. However, this explanation would not account for the symmetric structure observed at comparable distances in the large-sphere experiments.

The most likely explanation for the asymmetry is that dynamics close to the sphere act to weaken the amplitude of waves emanating along the bottom flank of the upper wave cone. Wave–wave interactions, as well as the dynamics of waves interacting with viscous boundary layers surrounding the sphere, are not described by the linear theory prediction derived in §2. Where the bottom flank of the upper wave cone meets the sphere, it interferes destructively with the lower wave cone while also interacting with the viscous boundary layer. This combination of interactions could act to decrease the amplitude of the bottom flank relative to the top flank. Though a theoretical investigation of this hypothesis is beyond the scope of this paper, we show below how the experimental results qualitatively distinguish the relative importance of wave–wave interactions and viscous effects.

At $r/a = 8$ (figure 8b), the three experimentally measured wave beams exhibit unimodal behaviour. Though theory predicts the beams should still be bimodal at this distance (where $d \simeq 0.013$), the slope of the amplitude envelope is small over a range of $\sigma < |a|$. Thus, even if the peaks occur in experiments, they may not be evident over the signal noise.

A consistent result in all three experiments is that theory, given by (2.15), moderately overpredicts the amplitude of the waves. This is illustrated more clearly in figure 9 which shows along-beam cross-sections at $\sigma = 0$ and $\sigma = a$ and compares these with theory. Both graphs show the $\langle \Delta N^2 \rangle$ field normalized by A_{N^2} and plotted against the non-dimensional distance d.

The decreasing amplitude along both cross-sections is captured well by theory. Along $\sigma = 0$, theory generally overpredicts the amplitude by 10 to 20%. The agreement between theory and experiment is particularly good along $\sigma = a$. By finding the best-fit line between $d = 0.01$ and 0.02 to the corresponding log–log plots of the theoretical curve, we find the amplitude decreases as d^{-p} ($\propto r^{-p}$) where $p = 0.998 (\pm 0.001)$. Averaging together the three normalized experimental curves we find the best-fit power law exponent gives $p = 1.01 (\pm 0.14)$. Both theory and experiments show that the amplitude along $\sigma = a$ drops off faster than $r^{-1/2}$ as a result of viscous attenuation of the wave beam. By examining the intercept of the best-fit lines, we find that theory overpredicts the amplitude of the waves by 35%.

We compare the results of the experiments with the small sphere to those with the large sphere by examining the corresponding across-beam cross-sections at $r/a = 5$ and $r/a = 8$. The normalized experimental data is compared with theory in figure 10.

Near the sphere, the wave beam clearly exhibits a bimodal structure and, unlike the small-sphere case, the structure here is symmetric. This is consistent with the discussion above in which we argue that dynamics near the sphere are responsible for the asymmetry in the small-sphere case. The large-sphere experiment demonstrates
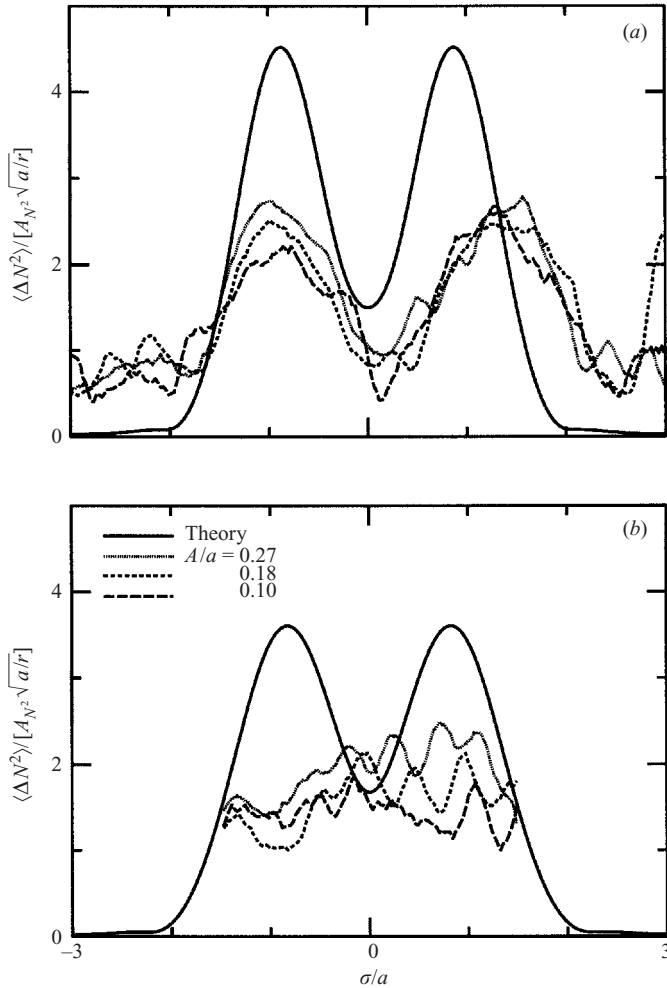
FIGURE 10. As in figure 8 but for the large sphere oscillating at three different amplitudes. Cross-sections are taken at (a) $r/a = 5$ ($d = 0.00287$) and (b) $r/a = 8$ ($d = 0.00459$).

that wave–wave interactions alone are not the likely cause, since asymmetry would be even more evident in this case. Instead, it is reasonable to deduce that the asymmetry results from wave interactions with the viscous boundary layer near the sphere. These dynamics are more pronounced for the small-sphere experiments since the Reynolds number $\mathrm{Re} \equiv Aa\omega/\nu$ (which ranges from 18 to 49) is less than half the corresponding value for the large-sphere experiments. Furthermore, the relative viscous boundary-layer thickness for the small-sphere experiments is almost double that for the large-sphere experiments. From scaling theory, the boundary-layer thickness is given approximately by $\delta_\nu \sim (\nu/\omega)^{1/2}$. In the small-sphere experiments, $\delta_\nu/a \simeq 0.07$. Although a small fraction, it is significant compared to the width of the two bimodal beams near the sphere.

Another distinguishing feature of the experimental results shown in figure 10(a) is that theory overpredicts the peak amplitude at $r/a = 5$ approximately by a factor 2. This is also true at $r/a = 8$, as shown in figure 10(b). Because the data correspond to a radial distance near the edge of the camera's field of view, the experimental data
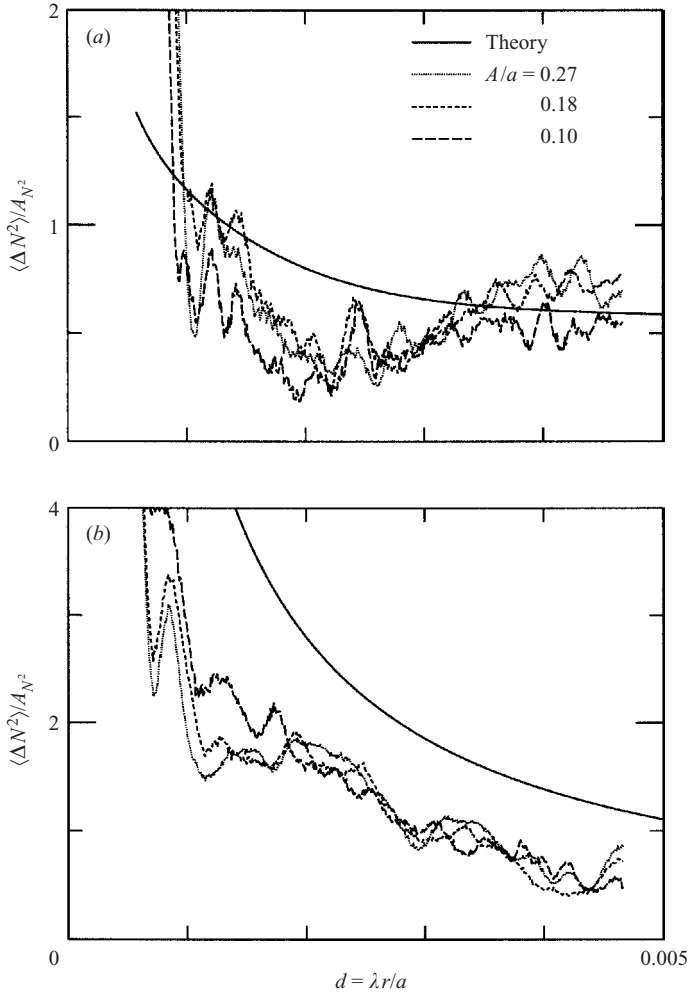
FIGURE 11. Comparison between the theoretical and experimental profiles of the $\langle \Delta N^2 \rangle / A_{N^2}$ field along the slice (a) $\sigma = 0$ and (b) $\sigma = a$ for large-sphere experiments.

are given only over the restricted range $-1.5 \leqslant \sigma/a \leqslant 1.5$. Nonetheless, the results show that this far from the sphere, the experimental data no longer exhibit bimodal behaviour, although theory predicts the profile should remain sharply peaked. These results demonstrate that theory does not accurately capture the dynamics of viscous attenuation near the sphere.

Consistent with these results, figure 11(a) shows that the along-beam amplitude at $\sigma = 0$ exhibits a distinct minimum near $d = 0.002$, whereas theory predicts the amplitude should decrease monotonically. The amplitude increases along $\sigma = 0$ for $d \gtrsim 0.002$ because viscous attenuation brings the peaks of the bimodal wave beams together over such a short distance that the amplitude increase in response to the merger occurs with a power-law dependence greater than $r^{-1/2}$. From figure 11(b), we determine the slope of the best-fit line between $d = 0.002$ and 0.005 to the log–log plot of the theoretical curve and find, as in the case of the small sphere, that the amplitude
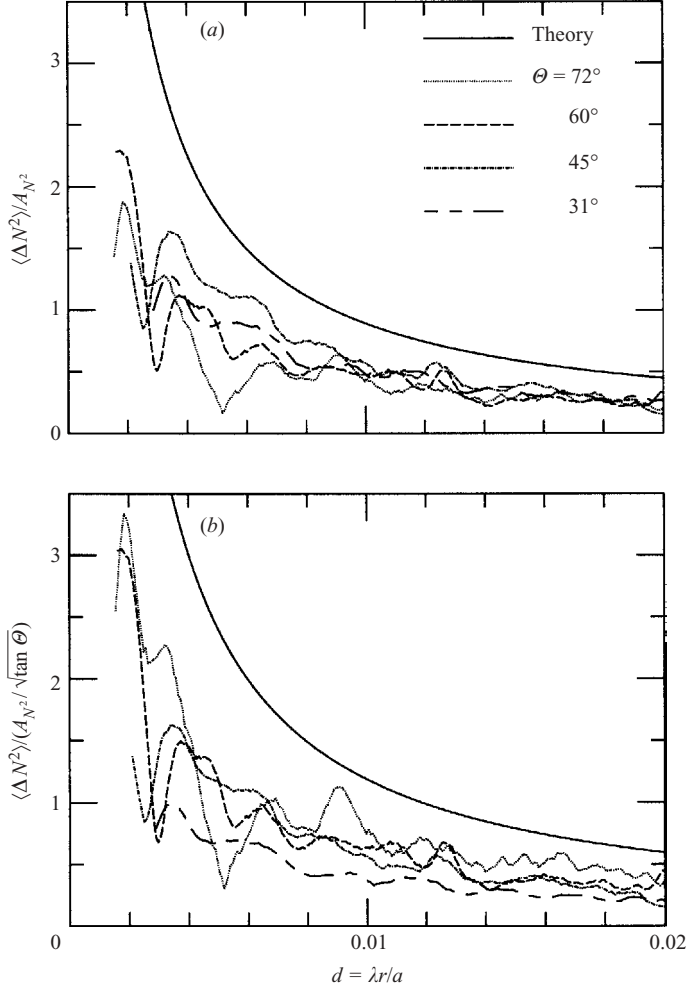
FIGURE 12. (*a*) Comparison between the theoretical and experimental profiles of the $\langle \Delta N^2 \rangle / A_{N^2}$ field along the slice $\sigma = -a$ for small-sphere experiments with different oscillation frequencies, as indicated by the values of Θ shown. (*b*) Comparison of same data but with amplitudes normalized by $(\tan \Theta)^{1/2}$.

decreases as d^{-p} with $p = 1.01 \, (\pm 8 \times 10^{-5})$. However, the averaged experimental data give a larger power law over this range. We find $p = 1.49 \, (\pm 0.15)$.

4.3. *Frequency dependence*

Figure 12 compares the results of experiments in which the small sphere oscillates at fixed relative amplitude $A/a = 0.26$, but with a range of frequencies. The normalized $\langle \Delta N^2 \rangle$ field is shown along the slice $\sigma = -a$, on the lower flank of the upper wave cone. This cross-section is selected because it lies on the outside edge of the upper wave cone, a region with a strong signal that is least affected by surface reflections and wave interference within the wave cone. As in figure 9, figure 12(*a*) shows the data in which $\langle \Delta N^2 \rangle$ is normalized by A_{N^2} and the along-beam distance r is normalized by a/λ. As a result of scaling by these Θ-dependent factors, the experimental data
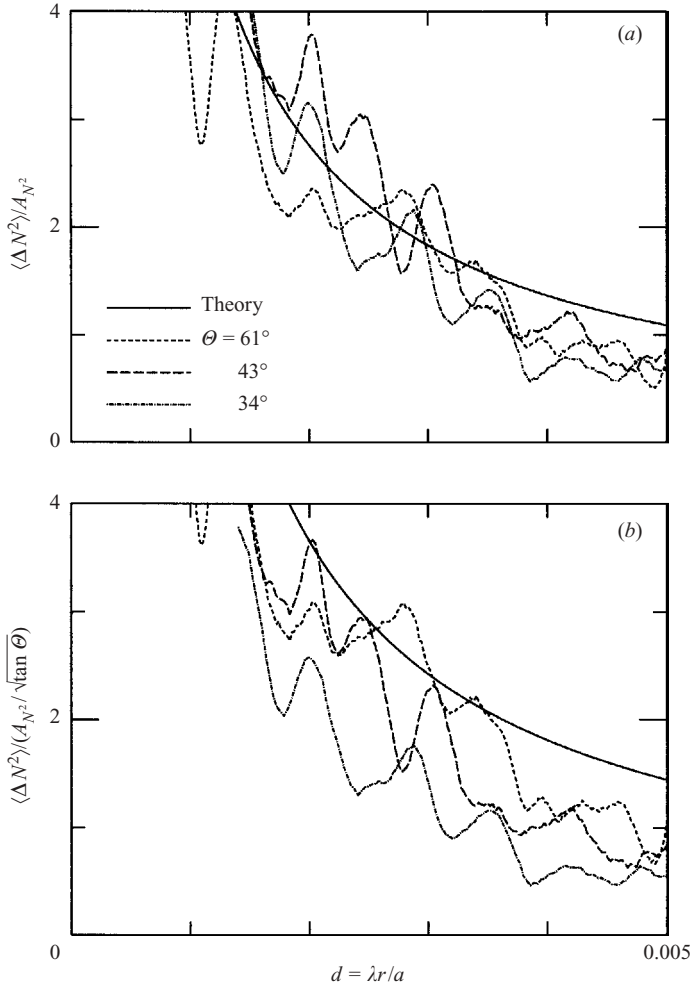
FIGURE 13. As in figure 12, but for experiments with large sphere.

collapse remarkably well onto a single curve. The agreement is particularly good for $d > 0.01$.

In comparison, figure 12(b) shows that the same data collapse less well when $\langle \Delta N^2 \rangle$ is normalized by $A_{N^2}/(\tan \Theta)^{1/2}$, which is the scaling factor that arises from the inviscid theory that predicts that the streamfunction is given by (2.3).

The same conclusions hold for experiments with the large sphere. As in figure 12, figure 13 shows the corresponding results from experiments with $a = 3.2$ cm and $A/a = 0.26$. When scaled by A_{N^2}, the data collapse better onto a single curve, particularly for $d > 0.003$.

Thus, despite invoking the boundary-layer approximation and despite heuristically matching boundary conditions by extrapolating the far-field results to the sphere surface, the theoretical prediction given by (2.15) correctly predicts the far-field amplitude of the wave beam to within a constant empirical factor moderately larger than unity.

5. Conclusions

We have derived and analysed a formula for the structure of small-amplitude Boussinesq internal wave cones generated by a vertically oscillating sphere. Unlike the corresponding formula for an oscillating circular cylinder, this theory predicts that the centreline amplitude of the beam, as measured by the ΔN^2 field, decreases monotonically over its extent. The theory neglects the dynamics of viscous boundary layers surrounding the sphere and it assumes along-beam variations are negligibly small.

We test the range of applicability of theory in experiments with spheres of two different sizes. By adapting synthetic schlieren to measure axisymmetric disturbances, we are able to measure non-intrusively wave amplitudes everywhere in space and time. Here, we have analysed the amplitude envelope since this reduces signal noise by constructing the root-mean-square average of many images.

Good agreement is found between theory and experiment for the small sphere. For relative oscillation amplitudes as large as 0.27, we find the theory moderately overpredicts the wave amplitude. The agreement is not as good as that in experiments with the large sphere. Theory overpredicts the amplitude of the wave cone by a factor of 2, and the wave beam changes from bimodal to unimodal structure over a shorter distance than that predicted by theory. For both small- and large-sphere experiments conducted with a range of frequencies, the data on the lower flank of the upper wave cone collapse best in the far field when scaled by a factor A_{N^2}, which is determined from the theory that employs the boundary-layer approximation. This theory consistently overpredicts the amplitude, presumably because it does not realistically match the boundary condition on the surface of the sphere and, in particular, because it does not account for the energy lost in the viscous boundary layer surrounding the sphere. Consistent with this assertion, we observe that the difference between theory and experiments is larger on the lower flank for experiments with the smaller sphere, which has a relatively larger viscous boundary layer.

The success of synthetic schlieren in non-intrusively measuring axisymmetric internal waves is encouraging. The results presented here inspire further study into the bimodal-to-unimodal transition as a function of sphere size, and the amplitude and frequency of the sphere's oscillation. In future work, the schlieren technique will be extended to examine fully three-dimensional disturbances by using inverse tomographic techniques applied to multiple perspectives through disturbances in a stratified fluid.

Appendix A. Velocity potential and streamfunction

Here, we show how to relate the velocity potential for internal wave cones to the streamfunction. This allows us to adapt the oscillating sphere results of Voisin (1991) so that they may be compared directly with the oscillating cylinder results of Hurley & Keady (1997) and Sutherland *et al.* (1999). Though Voisin (1991) used ψ to denote the velocity potential, here we denote it by ξ to distinguish it from the streamfunction, which is more typically denoted by ψ.
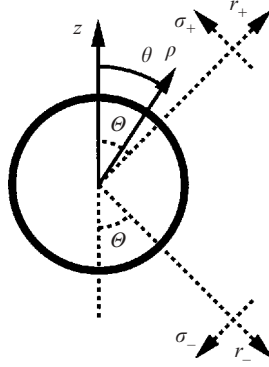
FIGURE 14. Orientation of upper and lower wave cone coordinate systems used to locate point at (ϱ, θ). The origin for each system is at the centre of the sphere.

For periodic waves, the velocity potential (which has units of length-squared multiplied by time) is related to pressure, p by (Voisin 1991)

$$p = i\omega\rho_0(N^2 - \omega^2)\xi. \tag{A 1}$$

We relate this to ψ using the radial component of Euler's equation for small-amplitude Boussinesq flow:

$$\frac{\partial u_R}{\partial t} = -\frac{1}{\rho_0}\frac{\partial p}{\partial R}. \tag{A 2}$$

Using (2.1) and the coordinate transformation (2.4), we find

$$\frac{\partial \psi}{\partial \sigma} = N^2 \sin\Theta \cos\Theta \frac{\partial \xi}{\partial \sigma}. \tag{A 3}$$

Integrating with respect to σ and requiring that ξ and $\psi \to 0$ as $\sigma \to \infty$ gives

$$\psi = \tfrac{1}{2}N^2 \sin 2\Theta\, \xi. \tag{A 4}$$

Applying this formula to (8.20) and (8.24) of Voisin (1991) yields (2.3).

Appendix B. Boundary conditions

Here, we show that the streamfunction given by (2.11) approximately satisfies the free-slip/no-normal-flow boundary conditions on the sphere.

We first evaluate the component of velocity of the upper wave cone normal to the sphere's surface at some arbitrary angle θ taken with respect to the z-axis, as shown in figure 14. This velocity is

$$u_{n+} = -\left.\frac{\partial \psi_+}{\partial \sigma_+}\right|_{\varrho=a} \cos(\Theta - \theta). \tag{B 1}$$

From figure 1(b), $\Theta \equiv \cos^{-1}(\omega/N)$. The point (ϱ, θ) is represented in along-beam, across-beam coordinates on the surface of the sphere by $(r_+, \sigma_+) = (a\cos(\Theta - \theta), a\sin(\Theta - \theta))$. In these formulae we have introduced the subscript '+', to distinguish the functions and parameters from those of the lower wave cone.

We use the following formula in the inviscid limit for the streamfunction of the upper (ψ_+) and lower (ψ_-) wave cone:

$$\psi_\pm(r, \sigma) \sim \pm\tfrac{1}{2}iAaN \cos\Theta \exp(-i\Theta)$$
$$\times \sqrt{\frac{a}{\varrho \exp[i(\Theta \mp \theta)]}} \int_0^\infty \frac{1}{K} J_{3/2}(K) \exp\left(\pm iK\frac{\sigma_\pm}{a}\right) dK. \quad (B\,2)$$

Note that along the upper wave cone in the limit $r_+ \gg a$, $\varrho \to r_+$ and $\theta \to \Theta$. Therefore, the formula for ψ_+ in (B 2) reduces to (2.11).

Taking σ_+-derivatives only within the integrand of (B 2) and using the explicit formula for the following definite integral

$$\int_0^\infty J_{3/2}(K)\,e^{iKx}\,dK = \frac{1}{\sqrt{1-x^2}}\left(\sqrt{1-x^2} + ix\right)^{3/2},$$

(B 1) gives

$$u_{n+} = \tfrac{1}{2}AN \cos\Theta\,e^{-i\theta}. \quad (B\,3)$$

Note, if we take the σ_+-derivative to include the σ_+-dependence of the factor $(\varrho \exp[i(\Theta - \theta)])^{-1/2}$, this results in a correction term of magnitude $\cos(\Theta - \theta)/3$ times the magnitude of (B 3). This is negligibly small near $\Theta - \theta = \pm\pi/2$ where the wave beam amplitude is largest (i.e. along the tangents to the sphere that form an angle Θ to the vertical).

Similarly, we evaluate the normal velocity u_{n-} due to the lower wave cone at the same position on the surface of the sphere: $(\varrho = a, \theta) \equiv (a \sin(\pi - \Theta - \theta), -a\cos(\pi - \Theta - \theta))$. We find

$$u_{n-} = \tfrac{1}{2}AN \cos\Theta\,e^{i\theta}. \quad (B\,4)$$

Combining (B 3) and (B 4), we find the normal velocity due to the superposition of the two wave cones is $u_n = AN \cos\Theta \cos\theta = A\omega \cos\theta$, which is exactly the normal component of the velocity of the sphere oscillating vertically with amplitude A and frequency ω.

Thus, within the accuracy of the boundary-layer approximation, the formula (2.11) is consistent with free-slip/no-normal-flow boundary conditions.

Though a more accurate formula could possibly be used, we have chosen to compare experimental data with (2.15), which is derived directly from (2.11), because of its similarity with the corresponding formula for the oscillating circular cylinder. Detailed analyses are performed sufficiently far from the sphere that the boundary-layer approximation is valid.

REFERENCES

APPLEBY, J. C. & CRIGHTON, D. G. 1986 Non-Boussinesq effects in the diffraction of internal waves from an oscillating cylinder. *Q. J. Mech. Appl. Maths* **39**, 209–231.

APPLEBY, J. C. & CRIGHTON, D. G. 1987 Internal gravity waves generated by oscillations of a sphere. *J. Fluid Mech.* **183**, 439–450.

BENDER, C. M. & ORSZAG, S. A. 1999 *Advanced Mathematical Methods for Scientists and Engineers.* Springer. 608 pp.

DALZIEL, S. B. 1992 Decay of rotating turbulence: some particle tracking experiments. *Appl. Sci. Res.* **49**, 217–244.

DALZIEL, S. B., HUGHES, G. O. & SUTHERLAND, B. R. 2000 Whole field density measurements. *Exps. Fluids* **28**, 322–335.

GRADSHTEYN, I. S. & RYZHIK, I. 1980 *Table of Integrals, Series, and Products.* Academic Press. 1160 pp.

GREENBERG, P. S., KLIMEK, R. B. & BUCHELE, D. R. 1995 Quantitative rainbow schlieren deflectometry. *Appl. Optics* **34**, 3810–3822.

HURLEY, D. G. 1997 The generation of internal waves by vibrating elliptic cylinders. Part 1. Inviscid solution. *J. Fluid Mech.* **351**, 105–118.

HURLEY, D. G. & KEADY, G. 1997 The generation of internal waves by vibrating elliptic cylinders. Part 2. Approximate viscous solution. *J. Fluid Mech.* **351**, 119–138.

IRVIN, B. R. & ROSS, J. 1991 Observations of pattern evolution in thermal convection with high-resolution quantitative schlieren imaging. *Phys. Fluids* A **3**, 1699–1710.

LIGHTHILL, M. J. 1960 Studies on magneto-hydrodynamic waves and other anisotropic wave motions. *Phil. Trans. R. Soc. Lond.* A **252**, 397–430.

LIGHTHILL, M. J. 1967 On waves generated in dispersive systems by travelling forcing effects, with applications to the dynamics of rotating fluids. *J. Fluid Mech.* **27**, 725–752.

LIGHTHILL, M. J. 1978 *Waves in Fluids.* Cambridge University Press. 504 pp.

MAKAROV, S. A., NEKLYUDOV, V. I. & CHASHECHKIN, Y. D. 1990 Spatial structure of two-dimensional and monochromatic internal-wave beams in an exponentially stratified liquid. *Izv. Atmos. Ocean. Phys.* **26**, 548–554.

MOWBRAY, D. E. 1967 The use of schlieren and shadowgraph techniques in the study of flow patterns in density stratified liquids. *J. Fluid Mech.* **27**, 595–608.

MOWBRAY, D. E. & RARITY, B. S. H. 1967a A theoretical and experimental investigation of the phase configuration of internal waves of small amplitude in a density stratified liquid. *J. Fluid Mech.* **28**, 1–16.

MOWBRAY, D. E. & RARITY, B. S. H 1967b The internal wave pattern produced by a sphere moving vertically in a density stratified liquid. *J. Fluid Mech.* **30**, 489–495.

ONU, K., FLYNN, M. R. & SUTHERLAND, B. R. 2003 Schlieren measurement of axisymmetric internal wave amplitudes. *Exps. Fluids* **35**, 24–31.

OSTER, G. 1965 Density gradients. *Sci. Am.* **213**, 70.

PRESS, W. H., FLANNERY, B. P., TEUKOLSKY, S. A. & VETTERLING, W. T. 1993 *Numerical Recipes: The Art of Scientific Computing.* Cambridge University Press. 702 pp.

STEVENSON, T. N. 1969 Axisymmetric internal waves generated by a travelling oscillating body. *J. Fluid Mech.* **35**, 219–224.

STEVENSON, T. N. 1973 The phase configuration of internal waves around a body moving in a density stratified fluid. *J. Fluid Mech.* **60**, 759–767.

SUTHERLAND, B. R., DALZIEL, S. B., HUGHES, G. O. & LINDEN, P. F. 1999 Visualization and measurement of internal waves by 'synthetic schlieren'. Part 1. Vertically oscillating cylinder. *J. Fluid Mech.* **390**, 93–126.

SUTHERLAND, B. R., HUGHES, G. O., DALZIEL, S. B. & LINDEN, P. F. 2000 Internal waves revisited. *Dyn. Atmos. Ocean* **31**, 209–232.

SUTHERLAND, B. R. & LINDEN, P. F. 2002 Internal wave excitation by a vertically oscillating elliptical cylinder. *Phys. Fluids* **14**, 721–731.

THOMAS, N. H. & STEVENSON, T. N. 1972 A similarity solution for viscous internal waves. *J. Fluid Mech.* **54**, 495–506.

VOISIN, B. 1991 Internal wave generation in uniformly stratified fluids. Part 1. Green's function and point sources. *J. Fluid Mech.* **231**, 439–480.

WEAST, R. C. 1981 *Handbook of Chemistry and Physics*, 62nd edn. CRC Press.